Research Article

Nanoscale viscoelastic transition from solid-like to liquid-like enables ductile deformation in Fe-based metallic glass

C.B. Jin [a,b,1], Y.Z. Wu [b,1], J.N. Wang [b], F. Han [b], M.Y. Tan [b], F.C. Wang [b], J. Xu [b], J. Yi [c], M.C. Li [a,*], Y. Zhang [b], J.T. Huo [b], J.Q. Wang [b,*], M. Gao [b,*]

[a] School of Materials Science and Engineering, Xinjiang Key Laboratory of Solid State Physics and Devices & School of Physical Science and Technology, Xinjiang University, Urumqi 830046, China
[b] CAS Key Laboratory of Magnetic Materials and Devices, and Zhejiang Province Key Laboratory of Magnetic Materials and Application Technology, Ningbo Institute of Materials Technology and Engineering, Chinese Academy of Sciences, Ningbo 315201, China
[c] Institute of Materials, School of Materials Science and Engineering, Shanghai University, Shanghai 200444, China

ARTICLE INFO

ABSTRACT

The cooling rate during vitrification is critical for determining the mechanical properties of metallic glasses. However, the structural origin of the cooling rate effect on mechanical behaviors is unclear. In this work, a systematical investigation of the cooling rate effect on the deformation mode, shear band nucleation, and nanoscale heterogeneous structure was conducted in three Fe-based metallic glasses. The brittle to ductile deformation transition was observed when increasing the cooling rate. Meanwhile, the governing shear band nucleation site from high load site to low load site appears the synchronous transition. By studying the corresponding nanoscale heterogeneous structure, it was found that nanoscale viscoelastic transition from solid-like to liquid-like as increasing cooling rate enables ductile deformation. The current work not only reveals the nanoscale structural origin of the cooling rate effect on the deformation behaviors, but also provides a new route to design ductile metallic glasses by freezing more nanoscale liquid-like regions during cooling.

© 2024 Published by Elsevier Ltd on behalf of The editorial office of Journal of Materials Science & Technology.

1. Introduction

Due to the unique atomic structure without long-range periodicity and the metallic bonding, metallic glasses (MGs) have exhibited a series of superior mechanical and functional properties, such as ultra-high strength, large fracture toughness, extraordinary catalytic properties, and superior soft magnetic properties [1–5]. These excellent physical properties make MGs have great potential in areas of aerospace, material molding, electric and electronic devices, and green hydrogen energy [1–5]. Especially, Fe-based soft magnetic MGs with higher saturation magnetic induction and lower core loss have become one of the best candidates for wireless charging, 5th-generation technology, and the next-generation power transformer core, which have received considerable attention [6,7]. On the other hand, as one type of metastable material, the glass structure and the mechanical properties of MGs are easily affected by various internal and external factors, such as the chemical composition, the cooling rate, the thermal history, and the rejuvenation treatment [8–14]. Among these factors, the cooling rate during materials preparation was thought to play a key role in the vitrification of MGs and the related dynamic behaviors of the relaxations, the crystallization, and the mechanical deformation behaviors [10,11,15–17]. For example, different cooling rates usually make Fe-based MGs display various nanocrystalline products with distinct soft magnetic properties. Lower cooling rates actually lead to embrittlement behavior and it seriously restrains their practical applications [18,19]. Although many experiments and simulation efforts have been made to investigate the cooling rate effect on the atomic structure and the mechanical properties in MGs [20–25], the physical mechanism for the cooling rate effect is still unclear due to the unknown atomic structure [26–30]. Therefore, it is critical to clarify the structural essence behind the cooling rate and build the bridge between the microscopic structure and the deformation behaviors of MGs.

For traditional crystalline alloy materials, the mechanical deformation behaviors are usually determined by the atomic scale, nanoscale, or micro-scale structural defects, such as the point de-

* Corresponding authors.
E-mail addresses: limingcan@xju.edu.cn (M.C. Li), jqwang@nimte.ac.cn (J.Q. Wang), gaomeng@nimte.ac.cn (M. Gao).
[1] These authors contributed equally to this work.

fects, the dislocations, and the grain boundaries [31,32]. In contrast, the carrier for the deformation behaviors in MGs is thought as the shear bands (SBs). The nucleation, propagation, and interaction of SBs directly lead to various deformation behaviors under external loading [1,33–36]. The thickness of SBs for various MG systems is about 10–20 nm and there exists one huge scale gap with the atomic packing structure [37,38]. To bridge the nanoscale SBs with the atomic structure, many researchers proposed a series of theoretical models, such as the shear transformation zone (STZ) model, the free volume model, and the flow unit model [39–41]. To some extent, these models can give semiquantitative explanations for some mechanical deformation behaviors and the qualitative physical picture for tuning the mechanical properties of MGs [1]. However, there is no quantitative model to connect the atomic structure with the nanoscale SB nucleation and the macroscopic deformation behaviors. On the other hand, a great deal of experimental researches showed that the viscoelastic structure of MGs at the nanoscale is not homogeneous. There exist two distinct viscoelastic modes of liquid-like and solid-like in various MGs [42–47]. The nanoscale liquid-like local regions with low modulus, low viscosity, and high atomic mobility have been verified to be the microscopic structural origin for the nucleation of SBs [38,48,49]. In addition, these nanoscale liquid-like regions have been suggested as the preferred sites that initiate the nucleation and crystallization, and the microscopic structure origin of the multiple relaxation processes [42,50,51]. These nanoscale liquid-like regions are similar to the structural defects in crystalline materials. It should be noted that, compared to the minor change of the atomic structure with distinct cooling rates, both the macroscopic physical properties and the nanoscale structural heterogeneity in MGs display a large and synchronous change [42,50,51]. This consistent change may imply that the nanoscale structural heterogeneities rather than the atomic packing structure are more closely related to the mechanical deformation behaviors. Thus, the nanoscale structural heterogeneities may provide a new perspective to uncover the physical mechanism of the cooling rate on the mechanical deformation behaviors in MGs.

In this work, to clarify the nanoscale structural origin of the cooling rate effect on the deformation behaviors, we specially selected three Fe-based MGs with great application potential as the research objects. The evolution of nanoscale structural heterogeneity, SB nucleation kinetics, and deformation behaviors with different cooling rates were systematically studied. Micropillar compression tests were conducted to determine the mechanical deformation behaviors with different cooling rates. The experimental strategy based on the nanoindentation tests [34,52,53] was applied to obtain information on SB nucleation kinetics including the nucleation site type, the nucleation site density, and the nucleation rate corresponding to different cooling rates. Static force microscopy (SFM) was used to detect the evolution of the nanoscale structural heterogeneities with different cooling rates. Finally, one physical scheme was proposed to illustrate the cooling rate effect and the intrinsic relationship of the nanoscale structural heterogeneity, the microscale SB nucleation behaviors, and the macroscopic deformation mode in MGs.

2. Experimental setup

2.1. Sample preparation and structural characterization

The ingots with the nominal chemical compositions of $Fe_{73.5}Si_{13.5}B_9Nb_3Cu_1$, $Fe_{82}Si_2B_{16}$, and $Fe_{36}Co_{36}B_{19.2}Si_{4.8}Nb_4$ were prepared by induction melting the mixture of pure Fe, Si, B, Nb, Co, and Cu with 99.9% purity in a high-purity argon atmosphere. To ensure chemical homogeneity, all of the ingots were re-melted at least six times. Then, the obtained ingots were cut into sev-

eral small pieces for the following procedures. For different Fe-based MGs, different samples were prepared by different fabrication methods. For $Fe_{73.5}Si_{13.5}B_9Nb_3Cu_1$, three different ribbon-like samples were prepared by single-roller melt spinning on a copper wheel with tangential speeds of 35, 40, and 45 m/s, respectively. The detailed fabrication process can be seen in the inserted scheme of Fig. 1(a). The ribbon-like samples corresponding to copper wheel speeds of 35, 40, and 45 m/s are marked as Glass 1, Glass 2, and Glass 3, respectively. The dimensions for the ribbon-like samples corresponding to the copper wheel speeds of 35, 40, and 45 m/s are 2 m × 2 mm × 47 μm, 2 m × 2 mm × 39 μm, and 2 m × 2 mm × 31 μm (length × width × thickness). Based on the method of estimating the cooling rate of amorphous alloys proposed by Lin and Johnson [54] (the detailed calculation process can be seen in part 1 of Supplementary Materials), the corresponding cooling rates of the above ribbon samples were calculated to be $(4.5 \pm 0.1) \times 10^5$, $(6.6 \pm 0.2) \times 10^5$, and $(10.2 \pm 0.1) \times 10^5$ K/s for copper wheel speeds of 35, 40, and 45 m/s.

Similarly, for $Fe_{82}Si_2B_{16}$, the melt spinning method was applied and the applied wheel speeds were 30, 40, and 50 m/s. The corresponding ribbon samples are labeled as Glass 4, Glass 5, and Glass 6. The dimensions for these ribbon-like samples corresponding to the copper wheel speeds of 30, 40, and 50 m/s are 2 m × 2 mm × 65 μm, 2 m × 2 mm × 35 μm, and 2 m × 2 mm × 20 μm (length × width × thickness). The corresponding cooling rates of the above ribbon samples were $(2.4 \pm 0.1) \times 10^5$, $(8.2 \pm 0.3) \times 10^5$, and $(25.1 \pm 1.2) \times 10^5$ K/s. For $Fe_{36}Co_{36}B_{19.2}Si_{4.8}Nb_4$, the ribbon-like and bulk samples were prepared by the melt spinning and copper mould suction casting methods. For bulk sample, one plate sample with the dimensions of 2 mm × 4 mm × 60 mm was obtained and was marked as Glass 7. For ribbon-like sample, the copper wheel speeds of 30 and 60 m/s were applied and the corresponding samples were marked as Glass 8 and Glass 9. For Glasses 7, 8, and 9, the corresponding cooling rates were 2.5×10^2, $(3.5 \pm 0.1) \times 10^5$ and $(16.1 \pm 0.6) \times 10^5$ K/s. The detailed results of the sample dimensions and the calculated cooling rates were included in Table S1 of Supplementary Materials. The glassy nature of the above-prepared samples was verified by X-ray diffraction (XRD, Bruker D8 Advance, Cu-K_α) and high-resolution transmission electron microscopy (HRTEM, Talos F200x).

2.2. Mechanical measurements

For ribbon-like samples with microscale thickness, the traditional mechanical measurement methods, such as compression, tension, and three-point bending tests, are not effective in characterizing the intrinsic mechanical deformation behaviors. In contrast, the micro-pillar compression test is a suitable and sensitive experimental tool to detect the evolution of the deformation behaviors with the cooling rate. Columnar samples for micro-pillar compression tests were fabricated from the as-cast ribbon-like MG samples by a focused ion beam system (FIB, FEI Helios-G4-CX). For bulk samples, to confirm the uniform experimental conditions, the micropillar samples of the same size were also prepared by FIB. To minimize the effect of FIB irradiation on the as-cast samples, the consecutive annular milling procedure with decreasing beam currents was applied. The detailed steps are: Firstly, one rough cutting is made with a high ion beam current of 9.3 nA. Secondly, grind out a groove that leaves an island in the center of the sample by an ion beam current of 2.5 nA. Finally, the micropillar samples are fabricated by gradually reducing the ion beam current to 0.79 nA. The dimensions for all of the fabricated micropillar samples are about 1 μm in diameter and 2–2.5 μm in height (the height-to-diameter ratio is between 2:1 and 2.5:1).
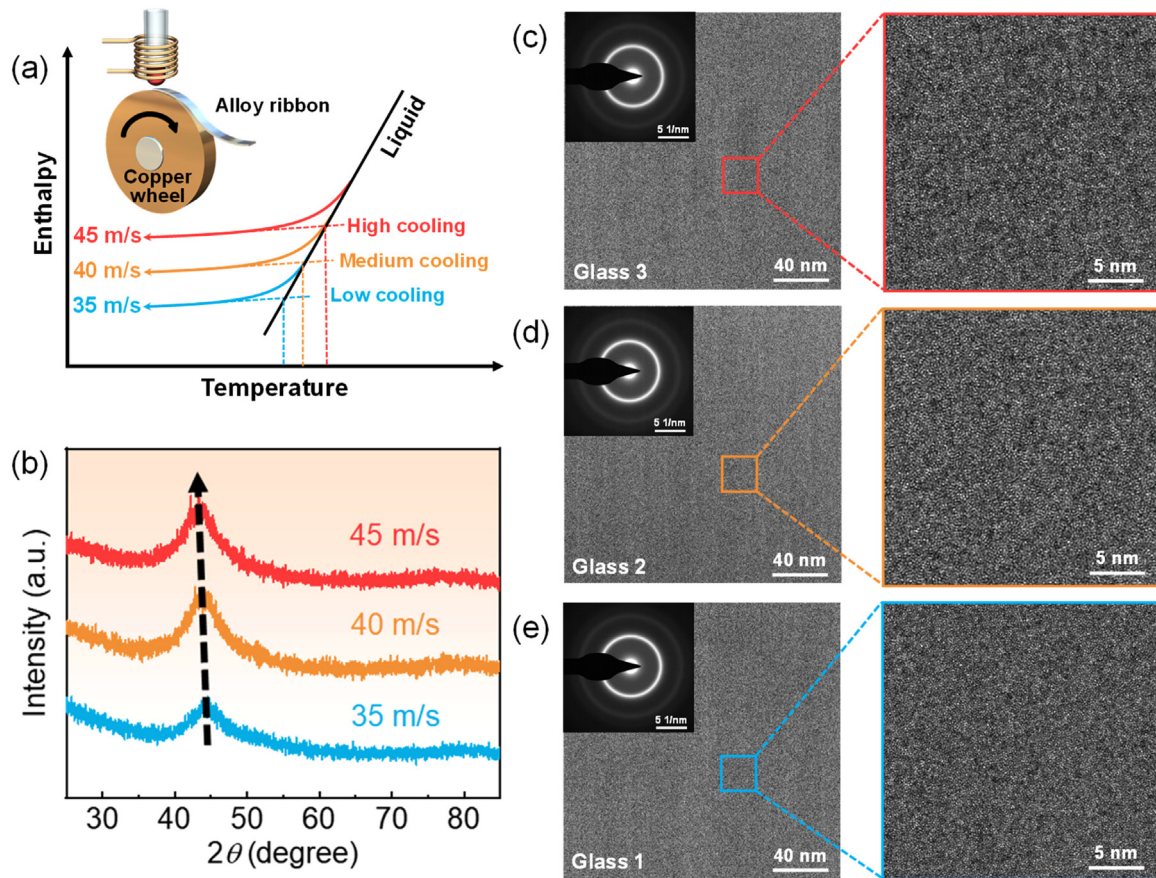
Fig. 1. (a) Scheme of glass formation cooling down from liquid with different cooling rates. The inset illustrates the experimental melt-spinning method to prepare the ribbon-like MG samples. (b) XRD patterns of the MG samples with different cooling rates. The black dashed arrow points to the evolution of the amorphous peak with the increase of the cooling rates. HRTEM images and the corresponding selected area electron diffraction patterns for MG samples with different cooling rates: (c) Glass 3 with fast cooling rate, (d) Glass 2 with medium cooling rate, and (e) Glass 1 with low cooling rate.

Micropillar compression tests were carried out on a Hysitron TI980 nanoindenter (Bruker) under the displacement-controlled mode at room temperature. The applied compression tip was the diamond flat punch indenter (TI-0145). The nominal stress was defined by the compressive load divided by the area of the top end of micropillars. The nominal strain was the ratio of displacement to sample height. For all compression tests, the allowed thermal drift is less than 0.05 nm/s and the strain rate is controlled at 1×10^{-3} s^{-1}. To ensure the reproducibility of the experimental results, at least three micropillar samples for each cooling rate were prepared. To detect the change of surface morphology induced by compression deformation, the morphology of all of the micropillar samples before and after compression tests was characterized by a double-beam scanning electron microscope (FEI Helios-G4-CX).

2.3. Nanoindentation tests

Before nanoindentation tests, all of the ribbon-like MG samples corresponding to three cooling rates were first cut into several small pieces with a length of about 2 cm. Then, they were mounted into different rubber molds by mixing epoxy hardener and epoxy resin for at least 12 h. Finally, all mounted samples were progressively polished with diamond abrasive films of 20, 10, 5, 2, 1, and 0.5 μm. To ensure that the surface of the polished samples is a smooth plane without scratches, the polished samples were observed through a metallographic microscope (Axio Observer 5). Meanwhile, to exclude the effect of the surface residual stress on the nanoindentation tests, all of the polished samples were held

at room temperature for at least three weeks before the following tests.

Nanoindentation tests were performed on a KLA G200 nanoindenter equipped with a Berkovich tip. The curvature radius of the applied tip is about 100 nm. All tests were performed with the load-controlling mode with a loading rate of 0.025 mN/s. For each sample, a rectangular matrix containing more than 200 points was tested to ensure that the obtained data were statistically significant. To prevent the possible overlapping of strain fields between the neighboring indentations, each of the indentations was separated by a lateral distance of 20 μm. The maximum drift rate for all tests was controlled under 0.05 nm/s to ensure low signal noise.

2.4. AFM measurements

The measurements of the nanoscale structural heterogeneity of all the MG samples were performed on the atomic force microscope (AFM, Bruker Dimension ICON) with an advanced PeakForce Quantitative Nanomechanics (QNM) mode. The applied AFM tip was silicon with a curvature radius of about 3 nm and a force constant of about 40 N/m. Before measurements, the calibration procedure was performed by using a force curve obtained on the surface of a standard sapphire sample. The sensitivity coefficient of the AFM tip was determined by the thermal tuning method. For each sample, the scanning area was set to a square region of 200 nm × 200 nm. QNM adhesion maps were measured at a resolution of 512 × 512 pixels to ensure the accuracy of the experimental results. To prevent the effect of surface oxidation and air dust particles, the AFM measurements were conducted on the fresh sur-

face of the as-cast MG ribbons. Surface topography and adhesive force images were recorded automatically during the scanning procedures. It should be noted that the adhesive force was extracted from the withdrawing part of the measured force curves. The detailed determination method for the adhesive force by AFM Peak-Force QNM mode can be seen in Refs. [47,49]. All of the AFM measurements were conducted in the ultra-clean room condition with a temperature of 23 ± 1 °C and a relative humidity of 20 %.

3. Results and discussion

In this section, the $Fe_{73.5}Si_{13.5}B_9Nb_3Cu_1$ MG samples with different cooling rates were the representative research objects to be systematically studied. The detailed experimental results and discussions for this composition were displayed from part 3.1 to part 3.4. For $Fe_{82}Si_2B_{16}$ and $Fe_{36}Co_{36}B_{19.2}Si_{4.8}Nb_4$ MG samples, the correlation between mechanical behaviors and nanoscale structural heterogeneities will be verified in part 3.5. Finally, in part 3.6, the physical mechanism of this correlation in MGs will be unveiled.

3.1. Structural characterization for $Fe_{73.5}Si_{13.5}B_9Nb_3Cu_1$ MGs

The XRD patterns of three MG samples of $Fe_{73.5}Si_{13.5}B_9Nb_3Cu_1$ are shown in Fig. 1(b) and they clearly display a fully glassy structure without any crystalline signals. HRTEM was used to further confirm the fully amorphous micro-structure of the samples in Fig. 1(c–e). One can see the completely disordered arrangement of the atoms in HRTEM images and the corresponding halo rings of SAED patterns. For the chemical composition of $Fe_{73.5}Si_{13.5}B_9Nb_3Cu_1$, it is one typical Fe-based soft magnetic MG system and it can easily transform into the nanocrystalline material with nanocrystals under thermal treatments. Thus, it may appear the phase separation for this composition during the preparation process. To verify the existence of this possibility, three magnified TEM images were taken from Fig. 1(c–e). It is clear that there was no phase separation for all three MGs. Meanwhile, the detailed distributions of different chemical elements for the three MGs were obtained by electronic differential system (EDS), as displayed in Fig. S2(a–c). One can see that the distributions for all elements are very homogeneous and there is no obvious element segregation. What is more, by comparing the peak values of the first amorphous peak for three MG samples in Fig. 1(b), a decrease in the peak value can be found with the increase in the cooling rates. This result indicates the atomic packing of the MG sample becomes looser with the increase in cooling rate. Based on Refs. [23,27,30,46], the looser atomic packing structure is prone to cause the formation of multiple SBs and the appearance of ductile deformation behaviors.

3.2. Mechanical deformation modes for $Fe_{73.5}Si_{13.5}B_9Nb_3Cu_1$ MGs

For the micro-pillar compression tests, due to the shape constriction from the sample and the compression tip, the microscale pillar sample is difficult to appear the catastrophic failure just like the bulk sample. Thus, in this work, a strain of 20 % was chosen to display the deformation behaviors of three MG samples by compressing the micropillar with a flat indenter at a strain rate of 1×10^{-3} s^{-1}. During tests, the serrated flow behaviors and the average SB slip velocity V_s can be considered as the standard to separate different deformation modes [55,56]. For the serrated flow behaviors, the number of stress drop $N(\Delta\sigma)$ corresponding to one serrated flow event usually exhibits a positive correlation with the plastic deformation ability. For SB velocity, a slower SB velocity means a larger resistance to the SB propagation and then usually displays better plasticity [55,56].

Fig. 2(a–c) shows the post-deformation surface morphology of the three glasses and the corresponding stress–strain curves are also displayed in Fig. 2(d–f). From Fig. 2(a–f), one can clearly see that the MG samples with different cooling rates exhibit significantly different deformation behaviors. For Glass 1, the typical brittle deformation mode accompanied by the formation of only one single SB takes place and there is no plastic deformation. For Glass 2, several secondary SBs are generated during the compression deformation (see Fig. 2(b)). The corresponding compression stress–strain curve in Fig. 2(e) exhibits several large serrated flows resulting in the appearance of small plastic deformation. For Glass 3, there appears a large number of SBs on the sample surface as presented in Fig. 2(c). A series of dense and frequent serrated flow events can be found in the compression stress–strain curve (see Fig. 2(f)). The numbers of the stress drop during the serrated flows $N(\Delta\sigma)$ for three MGs were listed in Table 1.

What is more, based on the observed serrated flow events, the average SB slip velocity (V_s) can be estimated (the detailed calculations are shown in Eq. S2 and the experimental results are exhibited in Fig. S3) and also included in Table 1. Although the intrinsic plastic deformation strain cannot be obtained by the micropillar compression tests, the yield strength σ_y can be determined based on the stress-strain curves in Fig. 2(d–f) and included in Table 1. To clearly display the cooling rate effect on the deformation behaviors, we plotted the evolution of σ_y, $N(\Delta\sigma)$, and V_s with the cooling rate in Fig. 2(g). Clearly, the yield strength decreases from 6.8 GPa for Glass 1 to 3.8 GPa for Glass 3 with the increase of the cooling rate. This result indicates a softer MG sample can be obtained with a larger cooling rate, which is coincident with Refs. [23,26]. Moreover, the larger number of SBs on the sample surface, the more frequent serrated flow events and the slower V_s directly indicate a ductile deformation mode for Glass 3. In contrast, there appears a brittle deformation mode for Glass 1 with fewer SB, fewer serrated flows, and faster V_s. Thus, the above results show that there appears a deformation mode transition from brittle to ductile when increasing cooling rates.

It should be noted that the serrated flow behaviors during micropillar compression tests are actually different from those during macroscopic compression tests [1,36,37]. Due to the limited microscale size and the fixed down part for the micropillar sample, the propagation of the SBs formed on the top part of the micropillar is prone to stop when they contact the compression tip. Then, it is prone to reload and the micropillar sample reaches the yielding point again. This leads to the oblique serrated flow events rather than the normal vertical-like stress drop during macroscopic compression. What is more, it is interesting to find that the apparent zigzag-like SB pattern is in good agreement with the activation of multiple main and secondary SBs for Glass 3 in Fig. 2(c). This special SB pattern effectively avoids strain localization into one dominant SB and raises the large plastic deformation.

3.3. SB nucleation kinetics for $Fe_{73.5}Si_{13.5}B_9Nb_3Cu_1$ MGs

For the above deformation behavior being dependent on the cooling rate, the SBs as the main deformation units should appear a big change with the cooling rates. Different SB behaviors are usually controlled by the nucleation kinetics including the nucleation mode, the nucleation site density, and the nucleation rate. In the below, the detailed information of the SB nucleation kinetics with the cooling rate will be investigated.

3.3.1. Nucleation processes

Considering that the SB nucleation is stochastic and first pop-in events during nanoindentation correspond to independent SB nucleation events [34,52,53], the SB nucleation kinetics can be obtained by analyzing the massive independent first pop-in events
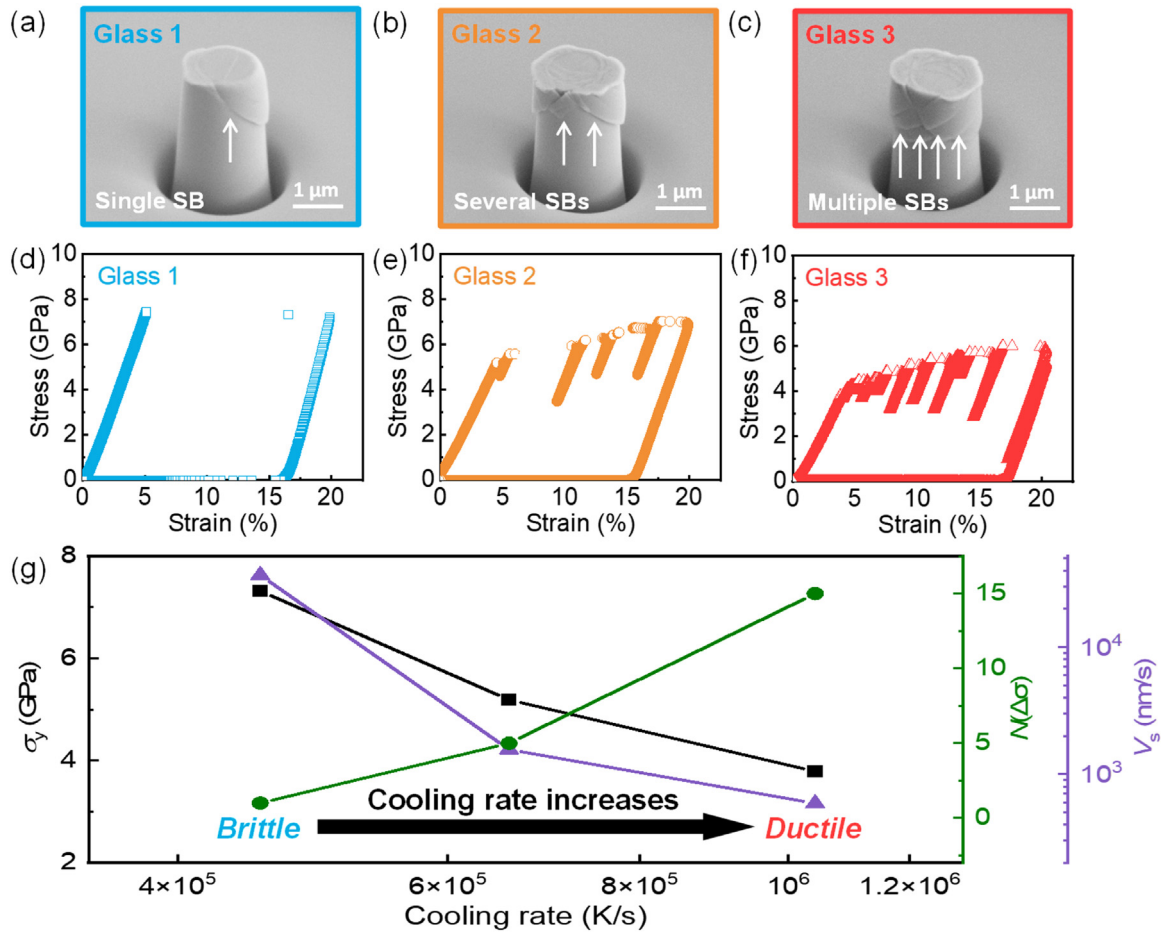
Fig. 2. Surface morphology for the post-deformation micropillar MG samples with different cooling rates: (a) Glass 1, (b) Glass 2, and (c) Glass 3. Micropillar compression stress-strain curves for MG samples with different cooling rates: (d) Glass 1, (e) Glass 2, and (f) Glass 3. (g) Plot of yield strength σ_y, average SB slip velocity V_s and number of stress drops for the serrated flows $N(\Delta\sigma)$ in MG samples with different cooling rates. The black arrow gives the transition from brittle deformation to ductile deformation with the increase of cooling rates.

Table 1

Data of ribbon thickness δ, cooling rate R_c, Young's modulus E_s, reduced elastic modulus E_r, Poisson's ratio ν_s, yield strength σ_y, number of stress drops for serrated flows $N(\Delta\sigma)$, and average SB slip velocity V_s for three Fe-based MG samples with different wheel speeds.

Composition	Sample	δ (μm)	R_c ($\times 10^5$ K/s)	E_s (GPa)	E_r (GPa)	ν_s	σ_y (GPa)	$N(\Delta\sigma)$	V_s ($\times 10^3$ nm/s)
$Fe_{73.5}Si_{13.5}B_9Nb_3Cu_1$	Glass 1	47±0.5	4.5 ± 0.1	268	234	0.301	7.3	1	36.9
	Glass 2	39±0.5	6.6 ± 0.2	260	229	0.302	5.2	5	1.6
	Glass 3	31±0.5	10.2 ± 0.1	255	225	0.304	3.8	15	0.6

with the statistically significant data. Fig. 3(a) displays the typical nanoindentation load and displacement curves with a loading rate of 0.025 mN/s for MG samples with different cooling rates. The black arrows point out the first pop-in events during continuous loading. For simplicity, Glass 3 was adopted to display the detailed experimental procedure and analyze the SB nucleation kinetics. Fig. 3(b) shows the scatter plot of the first pop-in load distribution based on about 200 independent nanoindentation tests for Glass 3. Clearly, the random distribution of the first pop-in loads verifies the stochastic process of the SB nucleation in MGs.

Then, the cumulative distributions of the first pop-in load for three MG samples with different cooling rates can be obtained and shown in Fig. 3(c). One can see that the cumulative distribution of the first pop-in load significantly shifts to a lower load range with the increasing cooling rate. This result implies an easier nucleation of the SB under a larger cooling rate [38,52]. According to the results in Fig. 3(c), the probability density functions of the first pop-in load distribution for MG samples with different

cooling rates can be determined and shown in Fig. 3(d). It can be seen that there exists an obvious shoulder on the high-load side of the peak rather than one typical symmetric Gaussian function for all three MG samples. In the following sections, the variation of the nucleation mode, the density of these two SB nucleation sites, and the nucleation rate with different cooling rates will be discussed.

3.3.2. Nucleation mode transition

For MGs, the character of bimodal SB nucleation sites is common and independent of the energy states and the chemical compositions. However, different MGs with different compositions or energies exhibit different SB nucleation behaviors and significantly distinct mechanical behaviors [34,52,53]. From Fig. 3(d), although the probability density distributions display a similar asymmetric character, the asymmetric distributions for the three MG samples are different considering different shoulder positions. To separate the dominated nucleation site during SB nucleation, the probabil-
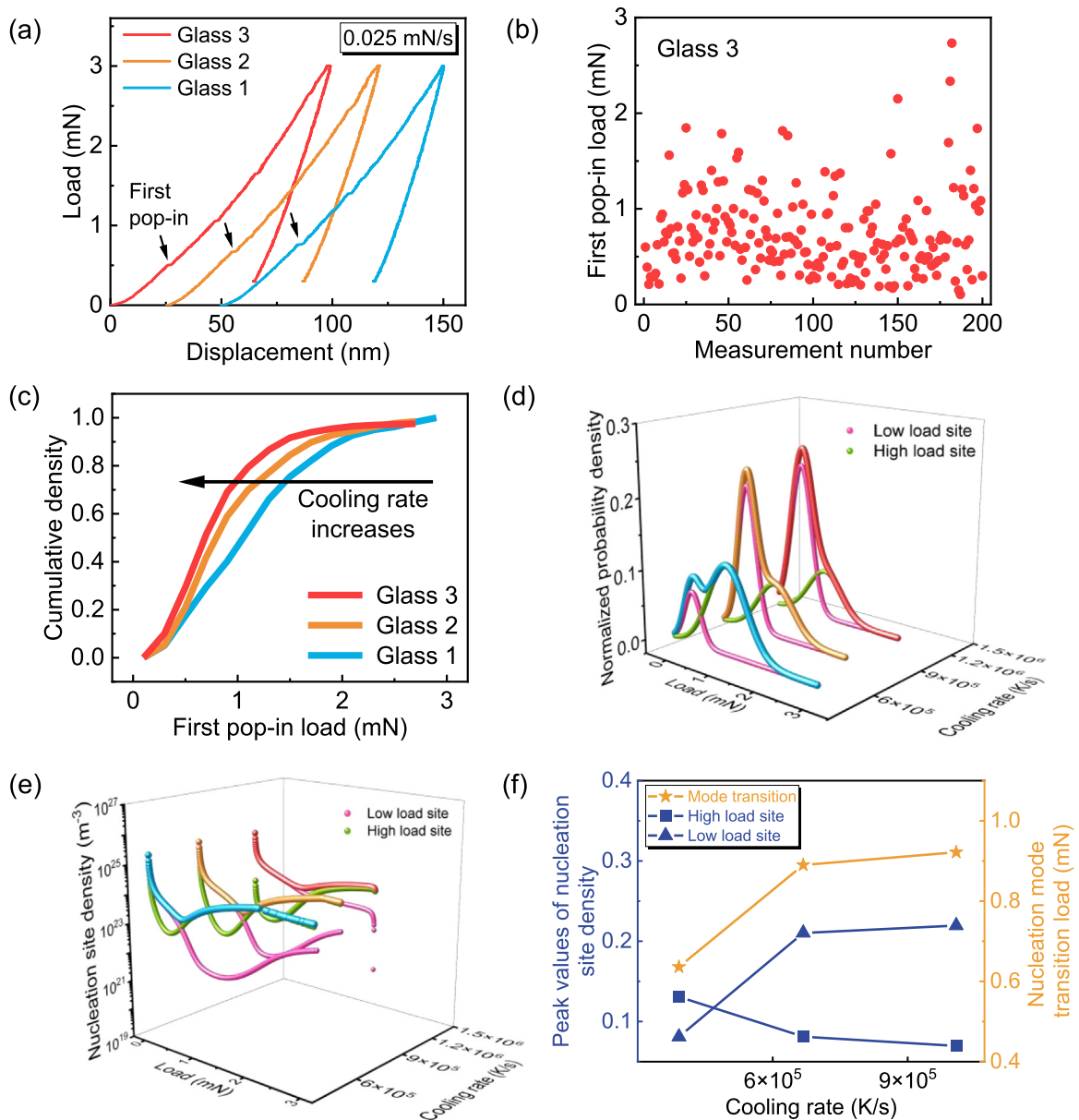
Fig. 3. (a) Typical nanoindentation load and displacement curves with the loading rate of 0.025 mN/s for MG samples with different cooling rates. The black arrows point out the first pop-in events during continuous loading. (b) Scatter plot of first pop-in load distribution based on about 200 independent nanoindentation tests for Glass 3. (c) Comparison of cumulative distributions of first pop-in load for MG samples with different cooling rates. The black arrow gives the increasing trend of the cooling rate. (d) Three-dimensional probability density functions of first pop-in load distribution for MG samples with different cooling rates. The magenta and green curves stand for the fitted Gaussian functions corresponding to two different SB nucleation sites. (e) Three-dimensional plot of the site densities for two SB nucleation sites versus load and cooling rate. (f) Evolution of peak values of the fitted nucleation site density functions for low-load and high-load modes, and the transition load for the governing nucleation site with cooling rates.

ity density functions of the first pop-in load for three MGs were fitted by two Gaussian functions in Fig. 3(d). Two well-fitted Gaussian functions directly indicate the existence of two SB nucleation sites in three MG samples. For simplicity, these two SB nucleation sites were marked as low-load site and high-load site. Moreover, one clear SB nucleation mode transition from the dominance of high-load site to the dominance of low-load site appears when increasing the cooling rate. Our previous work has shown that the dominance of low-load site during SB nucleation is prone to improve the plastic deformation ability [53]. Here, the high cooling rate induced SB nucleation mode transition from high-load site to low-load site is consistent with the above result of the ductile deformation for Glass 3 in Fig. 2.

3.3.3. Nucleation site density

For MGs, the more SB nucleation sites, the more SB forms, and then the larger the macroscopic plasticity [1,8–10,21,22,52]. Thus, the SB nucleation site density is the crucial parameter to understand the cooling rate effect on mechanical behaviors. According to the calculation method of SB nucleation site density based on the probability density distribution of the first pop-in load [35,52,53], the evolution of SB nucleation site density with different cooling rates can be determined and shown in Fig. 3(e). The detailed calculation process can be seen in Section 4 of Supplementary Materials. From Fig. 3(e), for three MG samples, the total SB nucleation site density function can be well-fitted with two Gaussian functions corresponding to two SB nucleation sites. What is more, for
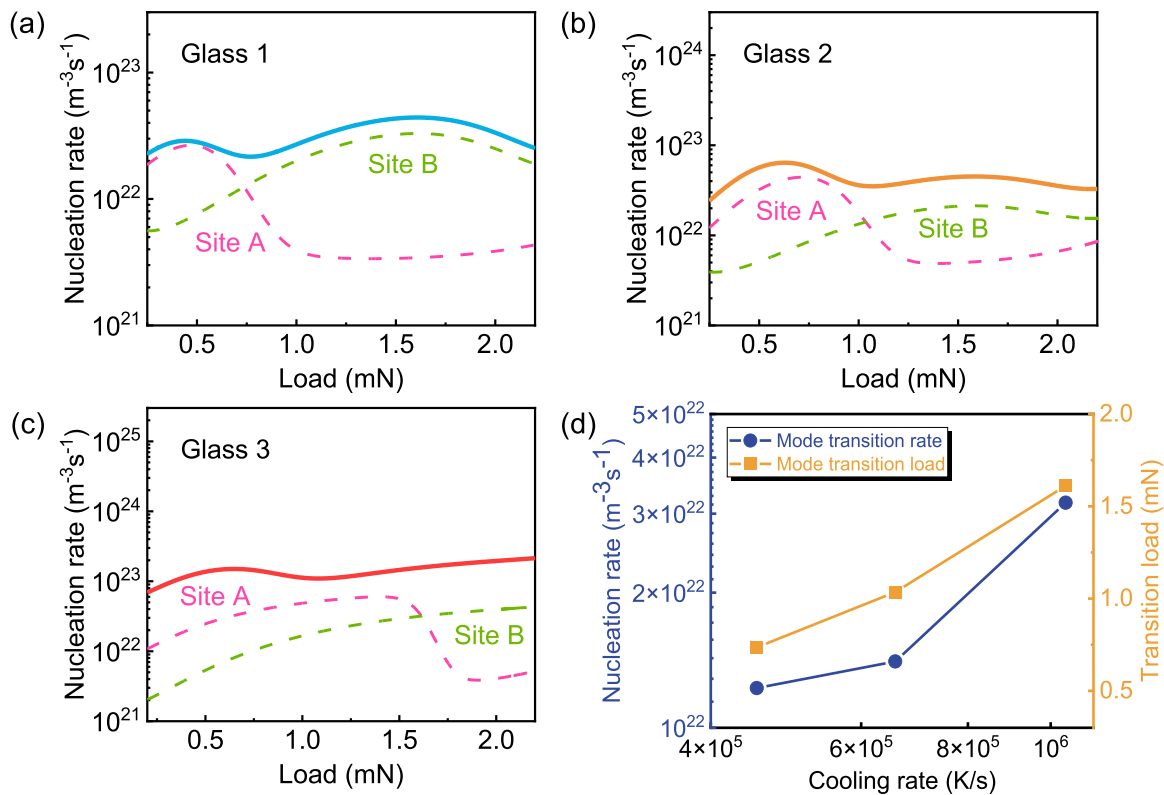
Fig. 4. Evolution of SB nucleation rate with load for MG samples with different cooling rates: (a) Glass 1 with low cooling rate, (b) Glass 2 with medium cooling rate, (c) Glass 3 with high cooling rate. The magenta and green curves are the fitted curves corresponding to low-load and high-load SB nucleation sites, respectively. (d) Evolution of nucleation rate and load at the SB nucleation mode transition point with cooling rates.

each SB nucleation site, there appears a transition from the low-load site governing to the high-load site governing as the external load increases. This implies that two nucleation sites separately control different stages during the SB nucleation process.

To quantitatively investigate the cooling rate influence on the SB nucleation site density, the peak values of the nucleation site density for two nucleation sites can be determined based on the results in Fig. 3(e) and shown in Fig. 3(f). Firstly, the peak values of the nucleation site density for two nucleation sites increase with the increasing cooling rate. This indicates higher cooling rate induces more SB nucleation sites. Secondly, a faster increase of the nucleation site can be found at the low-load site rather than the high-load site. The faster-increasing trend for low-load site means the nucleation rate behaves a larger sensitivity to the cooling rate than that of high-load site. In addition, the transition load between the low-load site and the high-load site was decided and shown in Fig. 3(f). One can see that the transition load shifts to the high load range with the increase in the cooling rate. This result implies that the higher cooling rate enhances the influence of low-load site within the wider external load range. In other words, more low-load sites will be activated under a higher cooling rate, which is beneficial for the improvement of the plasticity in MGs. The above result is also in line with the deformation behaviors in Fig. 2.

3.3.4. Nucleation rate

In view of the stochastic nucleation character, the SB nucleation rate can be obtained according to the classical nucleation theory and the Johnson–Samwer cooperative deformation model [34,52,53]. The detailed calculation process of the SB nucleation rate can be seen in section 5 of Supplementary Materials. Here, the variation of the SB nucleation rate with cooling rates is displayed in Fig. 4(a–c). Obviously, for all MGs with different cooling rates, the SB nucleation rate curve is also fitted by two Gaussian

functions corresponding to two nucleation sites, which are in line with the bimodal character of the SB nucleation density curve in Fig. 3(e). By comparing the initial nucleation rate without external load in Fig. 4(a–c), the nucleation rate displays an ascending trend as the cooling rate increases. This result implies a faster SB nucleation process for MG prepared by a higher cooling rate.

Moreover, for each nucleation rate curve, when the external load increases to a critical value, a transition of the governing nucleation site from the low-load site to the high-load site occurs. The transition load for three MG samples was plotted in Fig. 4(d). Clearly, the transition load is proportional to the cooling rate, which is similar to the dependence of the nucleation density on the cooling rate presented in Fig. 3(e). In addition, the nucleation rate at the transition load was also plotted in Fig. 4(d). A monotonous increase in the nucleation rate can be found with the increasing cooling rate. The above results further confirm a positive influence of the cooling rate on the nucleation and growth of SBs. Consequently, it can be concluded that a higher cooling rate will contribute to a larger SB nucleation site density and a faster SB nucleation rate, which therefore results in the formation of multiple SBs during deformation. This agrees well with the results demonstrated in Fig. 2.

3.4. Evolution of nanoscale structural heterogeneities with cooling rates for $Fe_{73.5}Si_{13.5}B_9Nb_3Cu_1$ MGs

3.4.1. Characterization of nanoscale structural heterogeneity

It is accepted that the intrinsic structure of MGs is usually heterogeneous in view of the asynchronous cooling within different local regions during vitrification. However, due to the limited experimental instruments, the detailed heterogeneous structure based on the atomic packing model is still unknown. In contrast, the nanoscale viscoelastic properties in the local regions,
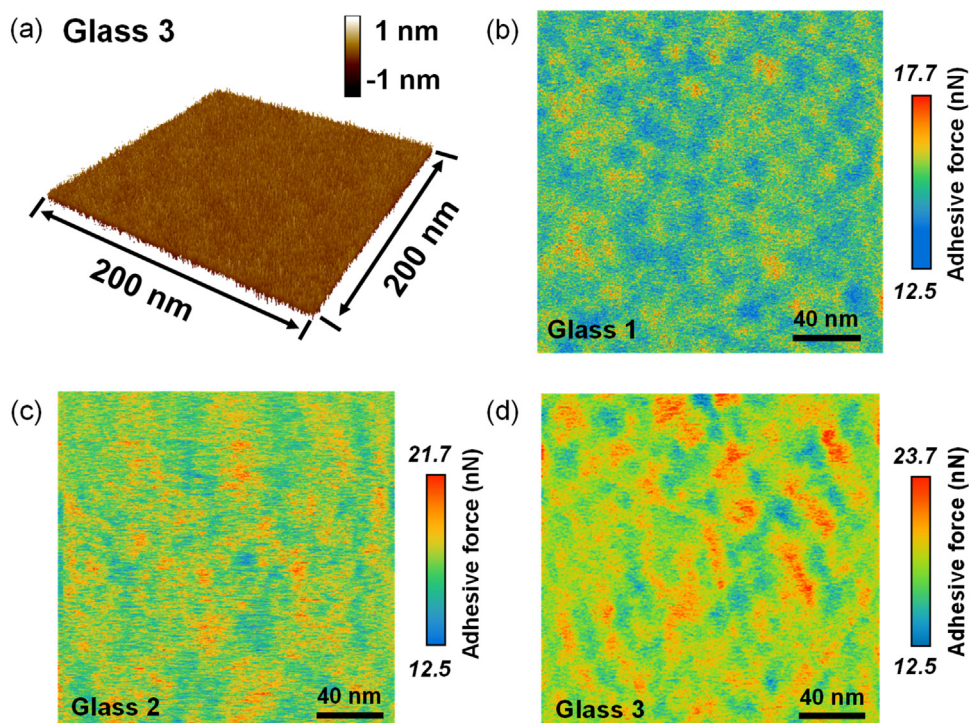
Fig. 5. (a) Three-dimensional surface topography of Glass 3 with high cooling rate. Two-dimensional spatial distributions of the local adhesive force for MG samples with different cooling rates: (b) Glass 1 with low cooling rate, (c) Glass 2 with medium cooling rate, (d) Glass 3 with high cooling rate.

such as the energy dissipation, the elastic modulus, and the adhesive force, seem to be more appropriate to display the intrinsic heterogeneous structures for MGs [42–47]. Thus, to investigate the microscopic structure origin for the cooling rate effect on the mechanical behaviors, the nanoscale heterogeneous structures with different cooling rates were characterized below. In this work, we used the scanning probe microscopy (SPM, AFM QNM mode) with the direct force curve measurement to detect the nanoscale viscoelastic structures under different cooling rates. To exclude the surface morphology effect on the measurements of the nanoscale viscoelastic properties, the surface roughness mappings for three MG samples were conducted. Fig. 5(a) shows the 3D map of the surface height difference for Glass 3 (The surface roughness information of other MGs is given in Fig. S4 of Supplementary Materials). One can clearly see that the surface height differences for all of three MG samples are within 1 nm and almost mirror-like. This low roughness makes sure that the surface morphology effect on the nanoscale viscoelastic measurements can be excluded.

For nanoscale viscoelastic properties, our previous works have suggested that the adhesive force is a more sensitive parameter for detecting the structural heterogeneity in MGs [47,49]. Thus, to more precisely detect the evolution of the structural heterogeneities with the cooling rates, the maps of the local adhesive force at the nanoscale for three MGs were obtained and displayed in Fig. 5(b–d). Evidently, different from the mirror-like surface topographies, all of the spatial distributions of the local adhesive force for three MG samples are not homogeneous. There exists a hierarchical structure consisting of soft regions (high adhesive force) and hard regions (low adhesive force), which is in conformity with previous reports [47,49]. For simplicity, these soft regions at the nanoscale are marked as liquid-like regions (LLRs) and the hard ones are marked as solid-like regions (SLRs) [47,49]. By comparing the scale bar of the adhesive force maps for three MGs, a positive dependence of the maximum value of the adhesive force on the cooling rate can be found. This result implies a larger influence of the cooling rate on the viscoelastic distribution of LLRs.

For Glass 1, the hierarchical viscoelastic structure can be considered as a model in that the LLRs embedded in the elastic matrix of the SLRs and the LLRs exhibit a small percentage. As to Glass 2, the percentage of the LLRs among the whole viscoelastic structure increases and it seems that the SLRs gradually transform into the LLRs. For Glass 3, the percentage of the LLRs is larger than that of the SLRs. The hierarchical viscoelastic structure has changed into a model of the SLRs embedded in the elastic matrix with the LLRs. In addition, the typical length of the LLRs increases from a few nanometers in Fig. 5(b) to tens of nanometers in Fig. 5(d) with the increase of the cooling rates. The larger cooling rate is prone to the formation of the larger LLRs and the viscoelastic mode transition appears when the cooling rate increases one critical value. Thus, the above result indicates that the change in the cooling rate leads to the transition of the whole viscoelastic mode for MGs.

3.4.2. Quantitative analyses of nanoscale structural heterogeneity

To quantitatively analyze the spatial distribution evolution of the nanoscale heterogeneous structures with the cooling rates, the probability density functions of the adhesive force corresponding to different cooling rates can be obtained based on the results in Fig. 5(b–d) and shown in Fig. 6(a–c). Clearly, the whole distribution of the adhesive force shifts into the higher value as the cooling rate increases, which means the softening behavior is induced by increasing the cooling rate. This result agrees well with the decrease of the elastic modulus when increasing the cooling rate in Fig. 2(d–f). What is more, the range of adhesive force probability distribution increases when increasing the cooling rate. A wider range of adhesive force means a more heterogeneous viscoelastic structure for MG with a higher cooling rate.

On the other hand, for the probability density functions of the adhesive force in three MGs, there seems a weak asymmetric character and the detailed fitting curves in Fig. 6(a–c). For all of the probability density functions for three MGs, it can be well fitted by two Gaussian functions, which indicates the existence of the double viscoelastic modes, i.e., the liquid-like and solid-like modes.
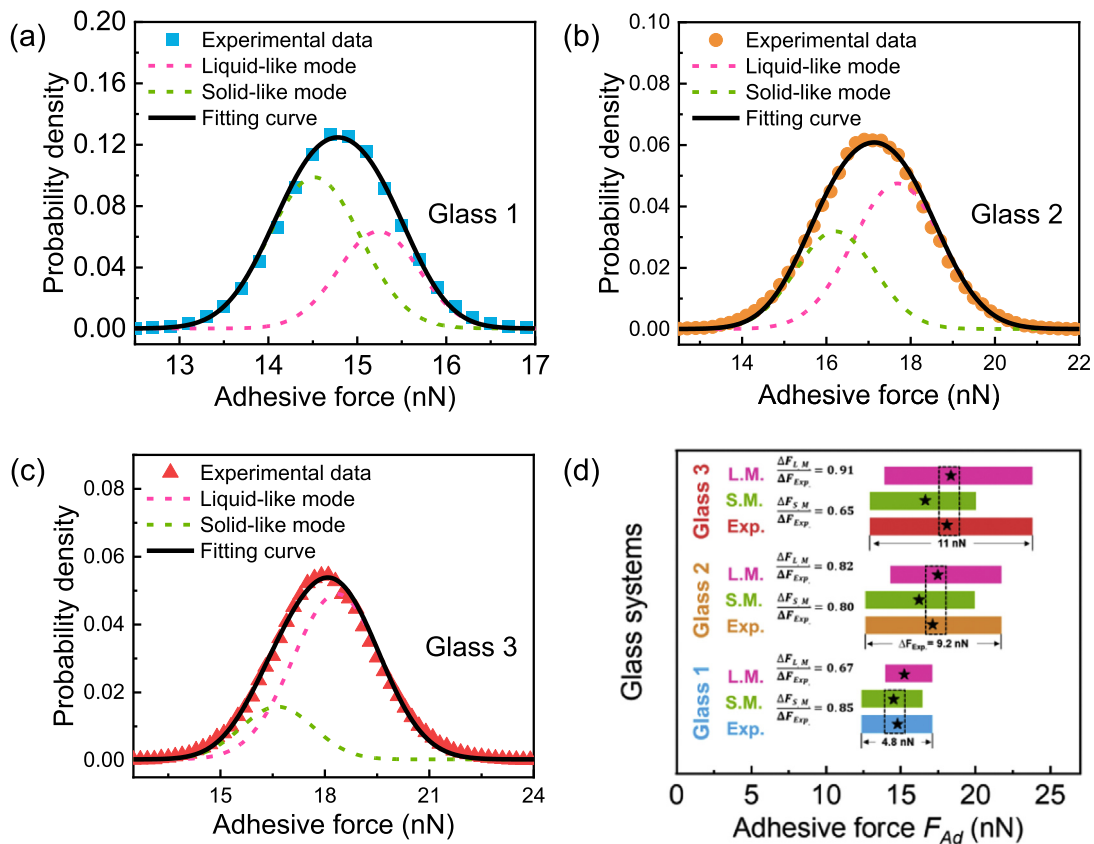
Fig. 6. Plots of the probability density distribution of the local adhesive force for MG samples with different cooling rates: (a) Glass 1 with low cooling rate, (b) Glass 2 with medium cooling rate, (c) Glass 3 with high cooling rate. The magenta and green curves stand for the fitted Gaussian functions corresponding to the liquid-like and solid-like viscoelastic modes, respectively. (d) Diagram of the adhesive force range of experimental data, the solid-like mode (S.M.), and the liquid-like mode (L.M.) for MG samples with different cooling rates. The black star points give the peak position of the probability density functions in (a–c). The black dashed rectangles mark the dominant viscoelastic mode for the experimental adhesive force distributions.

Moreover, for Glass 1, the solid-like mode plays a dominant role in the whole hierarchical structure. In contrast, the liquid-like mode governs the whole hierarchical structure in Glass 2 and Glass 3.

To more clearly exhibit the evolution of the hierarchical viscoelastic structure with the cooling rate, a diagram of the adhesive force ranges and the peak values of the probability distribution functions for the experimental data, the solid-like mode and the liquid-like mode with different cooling rates were displayed in Fig. 6(d). Firstly, one can clearly see that the adhesive force range increases from 4.2 nN for Glass 1, 8.3 nN for Glass 2 to 9.0 nN for Glass 3. A double-times increase in the range for Glass 2 and Glass 3 appears compared to that of Glass 1. A larger adhesive force range means a more heterogeneous structure [45,47,49,50]. Secondly, the peak values of the fitted liquid-like mode among the experimental probability distribution of Glass 2 and Glass 3 are larger than that of Glass 1. The ratio of liquid-like mode to experimental adhesion force range increases from 0.78, 0.88 to 0.90, while the ratio of solid-like mode to experimental adhesion force range decreases from 0.86, 0.82 to 0.64. The above results show the transition of the viscoelastic mode from solid-like mode dominance (Glass 1) to liquid-like mode dominance (Glasses 2 and 3). For the sake of clarity, the dominant viscoelastic mode was marked by the black dashed rectangles in Fig. 6(d).

Previous researches reported that the nucleation of SBs is closely related to the evolution of nanoscale LLRs under external loading [38–41,48,49]. Here, combing with the results of the SB nucleation kinetics with the cooling rate in Figs. 3 and 4, the bimodal SB nucleation sites of the low-load site and high-load site seem to be well coincident with the bimodal viscoelastic structures of the

liquid-like mode and solid-like mode. During deformation, the low-load nucleation sites with low activated energy are firstly activated from the LLRs with faster atomic mobility and lower modulus, and then the high-load nucleation sites will be stimulated from the SLRs when the applied load increases into one critical load. Moreover, it is interesting to find that the transition of the viscoelastic mode of the LLRs and SLRs with the cooling rate is in line with the transition of the deformation mode and the transition of the governing SB nucleation site. In view of the correspondence between the SB nucleation site and the viscoelastic structure, the increase of the percentage of the LLRs with the increase of the cooling rate will lead to the activation of more potential low-load SB nucleation sites. And more nucleation sites will arise the formation of more SBs and lead to slower SB propagation. Finally, the MG displays the ductile deformation mode. Thus, based on the above results and discussions, the cooling rate induced the transition of the deformation mode is originated from the evolution of the intrinsic nanoscale structural heterogeneity in MGs.

3.5. Verification of the correlation between nanoscale structural heterogeneities and deformation mode transition in other two fe-based MGs

The above results and discussions for $Fe_{73.5}Si_{13.5}B_9Nb_3Cu_1$ MGs have indicated that it is the nanoscale viscoelastic transition from solid-like to liquid-like that enables ductile deformation. In order to verify if this correlation exists in other Fe-based MGs, the mechanical behaviors and the nanoscale structural heterogeneities for $Fe_{82}Si_2B_{16}$ and $Fe_{36}Co_{36}B_{19.2}Si_{4.8}Nb_4$ MG samples with different
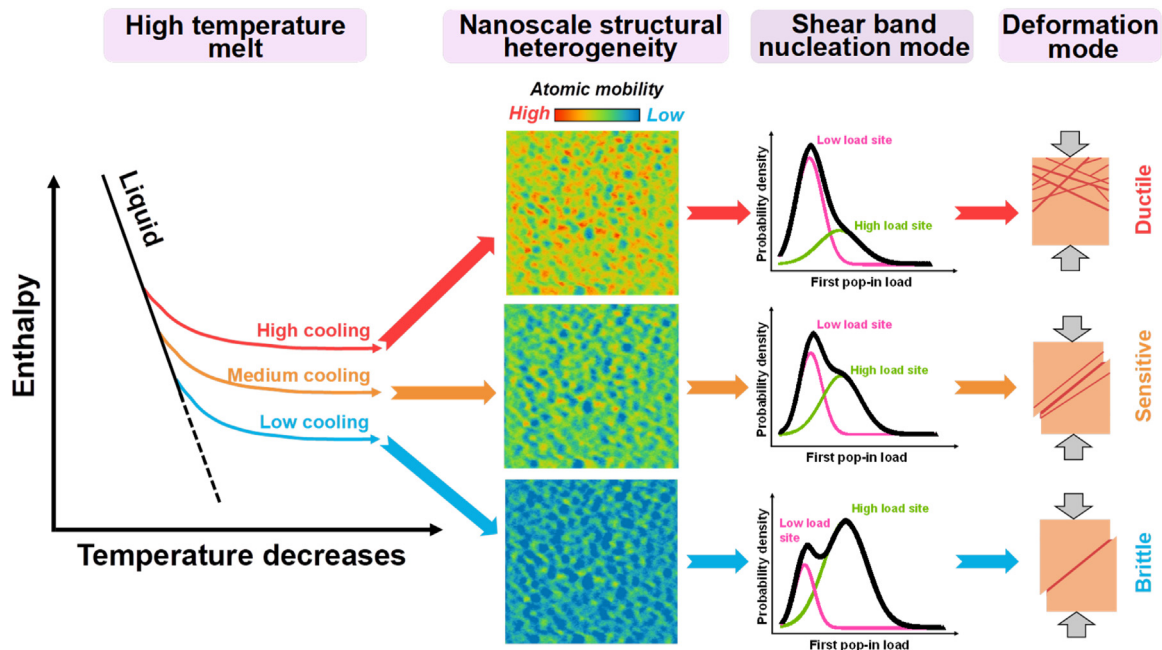
Fig. 7. Physical mechanism of cooling rate effect on the nanoscale heterogeneous structure, the microscale SB nucleation kinetics, and the deformation mode. High cooling rate induced the nanoscale viscoelastic transition enabling ductile deformation.

cooling rates were investigated. The detailed results of the structural characterization, mechanical behaviors and the nanoscale structural heterogeneities for these two MGs can be seen in section 7 of Supplementary Materials (See Figs. S5–S11). First, for two kinds of Fe-MGs with different cooling rates, there appears a similar transition of the deformation mode from ductile to brittle with the decrease of the cooling rates (See Figs. S6 and S7). Meanwhile, for the nanoscale structural heterogeneities, the viscoelastic mode transition from liquid-like to solid-like takes place with the decrease of the cooling rate (See Figs. S8–S11). The critical value of the cooling rate corresponding to the transition from the ductile mode to the brittle mode is the same as that of the transition from the liquid-like mode to the solid-like mode. What is more, to check the effect of cooling rate with larger differences, the bulk sample of $Fe_{36}Co_{36}B_{19.2}Si_{4.8}Nb_4$ MG was prepared and the cooling rate was about three orders of magnitude smaller than those of the ribbon-like samples (See Table S1). Clearly, the bulk sample displays the brittle deformation mode and the corresponding viscoelastic mode is solid-like, which is consistent with the results for the ribbon-like samples. Thus, the above results and discussions imply that the correlation between nanoscale structural heterogeneities and deformation mode transition does not depend on the detailed chemical composition of Fe-based MGs and the applied cooling rate range.

In this work, the correspondence between nanoscale structural heterogeneities and deformation mode transition was studied for three Fe-based MGs. Meanwhile, our previous work has reported that the transition of the SB nucleation mode corresponds to the ductile to brittle transition during structural relaxation in one Zr-based MG [53]. Recently, based on this work, we also investigated the corresponding evolution of the nanoscale structural heterogeneities for Zr-based MG. The viscoelastic mode transition from liquid-like to solid-like was accompanied by the ductile to brittle transition, which is very similar to the cooling rate induced by the deformation mode transition. Actually, different cooling rates endow the MGs with different energy states, which is equivalent to different structural relaxation states. Thus, when we apply for the proper cooling rate range, the ductile to brittle transition induced by the decrease of the cooling rate should be observed. In

our recent work, we have carried out the effect of cooling rate on the mechanical behaviors and nanoscale structural heterogeneities for this Zr-based MG. And a similar correlation has been found. The detailed experimental results will be included in our next manuscript.

3.6. Physical mechanism of the cooling rate effect on the deformation mode, the sb nucleation kinetics, and the nanoscale structural heterogeneity

For MGs, the cooling rate effect on the mechanical behaviors has been explained from the perspective of the relaxation, the energy state, or the free volume [12,15–19]. Based on the results and discussions in this work, the change of the cooling rate induced the deformation mode transition is actually accompanied by the transition of the SB governing nucleation site. Different from previous research, the current work found that the nanoscale heterogeneous viscoelastic structure appears an obvious change for the governing viscoelastic mode and the spatial topological distribution. Moreover, considering that the SB nucleates from the local viscoelastic regions, that is, the LLRs and SLRs, the double SB nucleation sites actually originate from the LLRs and SLRs. Thus, in view of the nanoscale structural heterogeneity, the mechanical behaviors and the SB nucleation kinetics can be well understood.

To more clearly illustrate the intrinsic correlation between the macroscopic deformation mode, the SB nucleation kinetics, and the nanoscale structural heterogeneity, a scheme of the physical mechanism for the cooling rate effect was proposed and shown in Fig. 7. According to this physical image, when being in the high-temperature melt, the mobilities for all of the atoms are very high and there should be small difference for their mobilities. During cooling down from the melt, the microscopic regions within the formed glasses with different cooling rates display different atomic mobility distributions. The local regions with high and low atomic mobility correspond to the LLRs and SLRs, respectively. Under external loading, both the LLRs and SLRs can be activated and transformed into the SB nucleation sites. LLRs are prone to produce the low-load nucleation sites and SLRs are prone to produce the high-load nucleation sites. Therefore, the MG sample with a high cool-

ing rate has a higher density of LLRs and then produces more low-load SB nucleation sites, which arises the formation of multiple SB and the macroscopic ductile deformation mode. On the contrary, the MG sample with a low cooling rate has a higher density of SLRs, and then produces more high-load SB nucleation sites, which only forms a few SBs and leads to the brittle deformation mode.

Different from the minor change of atomic packing structure under various external and internal factors, the nanoscale structural heterogeneities for MGs exhibit an obvious relationship with physical properties, such as the plastic deformation ability, the relaxation mode, and the soft magnetic property [18,46,56,57]. It seems that these nanoscale structural heterogeneities may be considered as the basic structural unit to tune the physical properties. It is similar to the role of point defects or dislocation defects in crystalline materials. Especially, considering that all kinds of mechanical properties for MGs are related to the nucleation, the growth, and the propagation of SBs, the direct correlation between the SB nucleation kinetics and the nanoscale structural heterogeneities in this work may mean that the nanoscale structural heterogeneities can be quantitatively adjusted to design the improved mechanical properties. For example, new ductile MG materials can be designed by freezing more LLRs during vitrification via increasing the cooling rate, especially for some intrinsic brittle systems, such as Fe- and Mg-based MGs.

In addition, the glass-to-liquid transition during heating is usually considered as the process where a series of the LLRs are first activated from the solid-like regions and then percolate into large liquid regions [41]. This behavior is very similar to the formation of SB under external loading [49]. Thus, the current hierarchical structure model with bimodal viscoelastic modes may provide a universal physical picture to understand the key issues in glass science. It should be noted that the nanoscale LLRs and SLRs detected by SPM display different static viscoelastic properties, such as the elastic modulus and the adhesive force. In contrast, the dynamic viscoelastic parameters, such as the activation energy spectrum for different heterogeneities should be more important considering that the LLRs and SLRs will evolve under different stimuli [41]. Recently, Song et al. [58] reported the universal exponential relaxation spectrum and there exists a series of relaxation units in glasses. In view of the hierarchical spatial distribution of the nanoscale structural heterogeneities in Fig. 5, the reported relaxation units may correspond to these nanoscale structural heterogeneities with different viscoelastic properties. The information on the activation energy spectrum for different structural heterogeneities will be of great importance for understanding the glass transition and complex relaxation, which will be our research focus in the future.

4. Conclusions

In conclusion, we systematically investigated the evolution of nanoscale viscoelastic structure, micro-scale SB nucleation kinetics, and macroscopic deformation mode with different cooling rates in three Fe-based MGs. It was found that the larger cooling rate makes the MGs behave the ductile deformation accompanying the formation of multiple SBs. Meanwhile, with the increase of the cooling rate, the SB nucleation mode changes from the high load mode into the low load mode and the viscoelastic mode changes from the solid-like mode to the liquid-like mode. It is surprising to find that three transitions for macroscopic deformation mode, microscale SB nucleation kinetics, and nanoscale viscoelastic mode with the cooling rate are synchronous. These results not only reveal the microscopic structural origin of the cooling rate effect on the macroscopic deformation behaviors, but also provide enlightenment for the improvement of the plastic deformation ability by introducing more LLRs to proliferate more SB nucleation

sites. More importantly, the current work may inspire researchers to develop new MG materials with improved mechanical properties by regulating nanoscale heterogeneous structure rather than the atomic packing structure.

Declaration of competing interest

The authors declare that they have no known competing financial interests or personal relationships that could have appeared to influence the work reported in this paper.

CRediT authorship contribution statement

C.B. Jin: Investigation, Methodology, Formal analysis, Resources, Writing – original draft. **Y.Z. Wu:** Methodology, Formal analysis, Resources, Writing – original draft. **J.N. Wang:** Formal analysis, Validation. **F. Han:** Formal analysis, Validation. **M.Y. Tan:** Methodology, Formal analysis. **F.C. Wang:** Validation. **J. Xu:** Validation. **J. Yi:** Methodology, Validation. **M.C. Li:** Conceptualization, Funding acquisition, Supervision, Writing – review & editing. **Y. Zhang:** Validation. **J.T. Huo:** Funding acquisition, Validation, Writing – review & editing. **J.Q. Wang:** Conceptualization, Funding acquisition, Project administration, Resources, Writing – review & editing. **M. Gao:** Conceptualization, Methodology, Funding acquisition, Supervision, Project administration, Resources, Writing – review & editing.

Acknowledgements

Data availability

Data will be made available on request.

Supplementary materials

Supplementary material associated with this article can be found, in the online version, at doi:10.1016/j.jmst.2024.01.026.

References

[1] C. Schuh, T. Hufnagel, U. Ramamurty, Acta Mater. 55 (2007) 4067–4109.
[2] A.L. Greer, E. Ma, MRS Bull. 32 (2007) 611–619.
[3] M.D. Demetriou, M.E. Launey, G. Garrett, J.P. Schramn, D.C. Hofmann, W.L. Johnson, R.O. Ritchie, Nat. Mater. 10 (2011) 123–128.
[4] M.X. Li, S.F. Zhao, Z. Lu, A. Hirata, P. Wen, H.Y. Bai, M. Chen, J. Schroers, Y. Liu, W.H. Wang, Nature 569 (2019) 99–103.
[5] F.C. Li, T. Liu, J.Y. Zhang, S. Shuang, Q. Wang, A.D. Wang, J.G. Wang, Y. Yang, Mater. Today Adv. 4 (2019) 100027.
[6] H.X. Li, Z.C. Lu, S.L. Wang, Y. Wu, Z.P. Lu, Prog. Mater. Sci. 103 (2019) 235–318.
[7] H. Li, A.D. Wang, T. Liu, P.B. Chen, A.N. He, Q. Li, J.H. Luan, C.T. Liu, Mater. Today 42 (2021) 49–56.
[8] F. Moitzi, D. Şopu, D. Holec, D. Perera, N. Mousseau, J. Eckert, Acta Mater. 188 (2020) 273–281.
[9] X. Yuan, D. Şopu, F. Moitzi, K.K. Song, J. Eckert, J. Appl. Phys. 128 (2020) 125102.
[10] R. Raghavan, P. Murali, U. Ramamurty, Acta Mater. 57 (2009) 3332–3340.
[11] T. Gheiratmand, H.R. Hosseini, P. Davami, F. Ostadhossein, M. Song, M. Gjoka, Nanoscale 5 (2013) 7520–7527.
[12] G. Kumar, P. Neibecker, Y.H. Liu, J. Schroers, Nat. Commun. 4 (2013) 1536.

[13] Q. Wang, J.J. Liu, Y.F. Ye, T.T. Liu, S. Wang, C.T. Liu, J. Lu, Y. Yang, Mater. Today 20 (2017) 293–300.

[14] S.V. Ketov, Y.H. Sun, S. Nachum, Z. Lu, A. Checchi, A.R. Beraldin, H.Y. Bai, W.H. Wang, D.V. Louzguine-Luzgin, M.A. Carpenter, A.L. Greer, Nature 524 (2015) 200–203.

[15] J.E.K. Schawe, J.F. Loffler, Nat. Commun. 10 (2019) 1337.

[16] L.J. Song, M. Gao, W. Xua, J.T. Huo, J.Q. Wang, R.W. Li, W.H. Wang, J.H. Perepezko, Acta Mater. 185 (2020) 38–44.

[17] Z.Y. Liu, Y. Yang, S. Guo, X.J. Liu, J. Lu, Y.H. Liu, C.T. Liu, J. Alloy. Compd. 509 (2011) 3269–3273.

[18] Z.Z. Yang, L. Zhu, L.X. Ye, X. Gao, S.S. Jiang, H. Yang, Y.G. Wang, J. Non-Cryst. Solids 571 (2021) 121078.

[19] Z.Z. Yang, S.S. Jiang, L.X. Ye, C. Zhu, X. Gao, H. Yang, Y.G. Wang, J. Non-Cryst. Solids 581 (2022) 121433.

[20] A. Hirata, T. Wada, I. Obayashi, Y. Hiraoka, Comm. Mater. 1 (2020) 98.

[21] X.X. Yue, C.T. Liu, S.Y. Pan, A. Inoue, P.K. Liaw, C. Fan, Physica B 547 (2018) 48–54.

[22] Y. Liu, H. Bei, C.T. Liu, E.P. George, Appl. Phys. Lett. 90 (2007) 071909.

[23] F. Li, H.J. Zhang, X.J. Liu, C.Y. Yu, Z.P. Lu, Comput. Mater. Sci. 141 (2018) 59–67.

[24] M. Wakeda, J. Saida, Comput. Mater. Sci. 218 (2023) 111930.

[25] D. Singh, R.K. Mandal, R.S. Tiwari, O.N. Srivastava, J. Alloy. Compd. 648 (2015) 456–462.

[26] D.B. Miracle, Nat. Mater. 3 (2004) 697–702.

[27] H.W. Sheng, W.K. Luo, F.M. Alamgir, J.M. Bai, E. Ma, Nature 439 (2006) 419–425.

[28] D. Ma, A.D. Stoica, X.L. Wang, Nat. Mater. 8 (2009) 30–34.

[29] K.J. Laws, D.B. Miracle, M. Ferry, Nat. Commun. 6 (2015) 8123.

[30] Y. Yang, J.H. Zhou, F. Zhu, Y.K. Yuan, D.J. Chang, D.S. Kim, M. Pham, A. Rana, X.Z. Tian, Y.G. Yao, S.J. Osher, A.K. Schmid, L.B. Xu, P. Ercius, J.W. Miao, Nature 592 (2021) 60–64.

[31] W.D. Callister Jr., D.G. Rethwisch, Materials Science and Engineering: An Introduction, 7th Edition, Wiley, New York, 2006.

[32] X.Y. Li, K. Lu, Nat. Mater. 16 (2017) 700–701.

[33] A.L. Greer, Y.Q. Cheng, E. Ma, Mater. Sci. Eng. R-Rep. 74 (2013) 71–132.

[34] J.H. Perepezko, S.D. Imhoff, M.W. Chen, J.Q. Wang, S. Gonzalez, Proc. Natl. Acad. Sci. U. S. A. 111 (2014) 3938–3942.

[35] R. Maaß, J.F. Löffler, Adv. Funct. Mater. 25 (2015) 2353–2368.

[36] H.B. Zhou, L.Q. Shen, B.A. Sun, W.H. Wang, J. Alloy. Compd. 955 (2023) 170164.

[37] C. Liu, V. Roddatis, P. Kenesei, R. Maaß, Acta Mater. 140 (2017) 206–216.

[38] D. Sopu, A. Stukowski, M. Stoica, S. Scudino, Phys. Rev. Lett. 119 (2017) 195503.

[39] F. Spaepen, Acta Metall. 25 (1977) 407–415.

[40] A.S. Argon, Acta Metall. 27 (1979) 47–58.

[41] Z. Wang, W.H. Wang, Natl. Sci. Rev. 6 (2019) 304–323.

[42] T. Ichitsubo, E. Matsubara, T. Yamamoto, H.S. Chen, N. Nishiyama, J. Saida, K. Anazawa, Phys. Rev. Lett. 95 (2005) 245501.

[43] J.C. Ye, J. Lu, C.T. Liu, Q. Wang, Y. Yang, Nat. Mater. 9 (2010) 619.

[44] Y.H. Liu, D. Wang, K. Nakajima, W. Zhang, A. Hirata, T. Nishi, A. Inoue, M.W. Chen, Phys. Rev. Lett. 106 (2011) 125504.

[45] P. Tsai, K. Kranjc, K.M. Flores, Acta Mater. 139 (2017) 11–20.

[46] F. Zhu, S.X. Song, K.M. Reddy, A. Hirata, M.W. Chen, Nat. Commun. 9 (2018) 3965.

[47] M. Gao, J.H. Perepezko, Nano Lett. 20 (2020) 7558–7565.

[48] J. Ding, S. Patinet, M.L. Falk, Y. Cheng, E. Ma, Proc. Natl. Acad. Sci. U. S. A. 111 (2014) 14052–14056.

[49] F. Xu, Y.Z. Liu, X. Sun, J.F. Peng, Y.H. Ding, J.T. Huo, J.Q. Wang, M. Gao, Appl. Surf. Sci. 611 (2023) 155730.

[50] F. Zhu, H.K. Nguyen, S.X. Song, D.P.B. Aji, A. Hirata, K.Nakajima H.Wang, M.W. Chen, Nat. Commun. 7 (2016) 11516.

[51] D.P. Wang, J.C. Qiao, C.T. Liu, Mater. Res. Lett. 7 (2019) 305–311.

[52] M. Gao, J.H. Perepezko, Mater. Sci. Eng. A 801 (2021) 140402.

[53] M. Gao, C. Kursun, J.H. Perepezko, J. Alloy. Compd. 952 (2023) 145556.

[54] X.H. Lin, W.L. Johnson, J. Appl. Phys. 78 (1995) 6514–6519.

[55] D.X. Hana, G. Wang, Q. Wang, R. Feng, X.D. Ma, K.C. Chan, C.T. Liu, Acta Mater. 152 (2023) 237–246.

[56] F.C. Li, M.X. Li, L.W. Hu, J.S. Cao, C. Wang, Y.T. Sun, W.H. Wang, Y.H. Liu, Adv. Sci. 10 (2023) 2301053.

[57] X. Wang, A. Datye, S. Zhang, J. Thornton, J. Schroers, U.D. Schwarz, Mater. Today Nano 22 (2023) 100346.

[58] L.J. Song, Y.R. Gao, P. Zou, W. Xu, M. Gao, Y. Zhang, J.T. Huo, F.S. Li, J.C. Qiao, L.M. Wang, J.Q. Wang, Proc. Natl. Acad. Sci. U. S. A. 120 (2023) e2302776120.